ACS APPLIED MATERIALS & INTERFACES

Research Article

Cite This: ACS Appl. Mater. Interfaces 2018, 10, 30680−30688

www.acsami.org

Preparation and Characterization of Chiral Transition-Metal Dichalcogenide Quantum Dots and Their Enantioselective Catalysis

Huan Zhang, Hui He, Xuemei Jiang, Zhining Xia, and Weili Wei*

School of Pharmaceutical Sciences and Innovative Drug Research Centre, Chongqing University, Chongqing 401331, P. R. China

Supporting Information

ABSTRACT: Two-dimensional transition-metal dichalcogenides (TMDs) had attracted enormous interests owing to their extraordinary optical, physical, and chemical properties. Herein, we prepared for the first time a series of chiral TMD quantum dots (QDs) from MoS_2 and WS_2 bulk crystals by covalent modification with chiral ligands cysteine and penicillamine. The chiral TMD QDs were carefully investigated by spectroscopic and microscopic techniques. Their chiral optical activity was confirmed by distinct circular dichroism signals different to those of the chiral ligands. Interestingly, with the assistance of copper ions, the chiral QDs displayed strong and chiral selective peroxidase-like activity. Up to now, inorganic nanomaterials with peroxidase-like activity were tremendous but seldom examples with enantioselectivity. The enantioselectivity of our chiral TMD QDs toward chiral substrates D- and L-tyrosinol was highly up to 6.77, which was almost the best performance ever reported. The mechanisms of enantioselectivity was further investigated by quartz crystal microbalance assays. We believed that because of the extraordinary electronic and optical properties, the chiral TMD QDs should be useful for nonlinear optical materials, asymmetric catalysis, chiral and biological sensors, and so on.

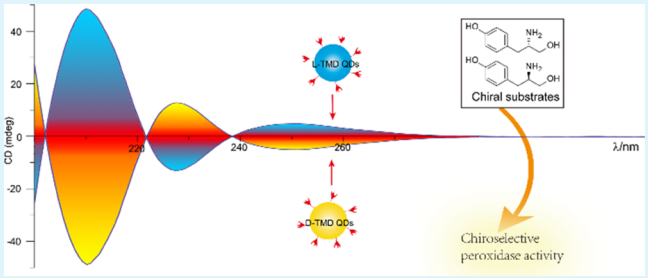

KEYWORDS: *chirality, nanozyme, transition-metal dichalcogenide, quantum dot, enantioselective catalysis*

1. INTRODUCTION

Excited by the tremendous investigation of graphene,[1,2] other graphene-like two-dimensional (2D) layered nanomaterials[3,4] such as hexagonal boron nitride,[5] graphitic carbon nitride,[6] and transition-metal dichalcogenides (TMDs)[7] have attracted enormous interests because of their extraordinary optical, physical, and chemical properties. Among them, the layered TMDs (e.g., MoS_2, $MoSe_2$, WS_2, and WSe_2), ranging from semiconductors and semimetals to true metals,[8] possess strong in-plane bonding and weak out-of-plane interactions enabling exfoliation into mono or few 2D layers.[9] Each TMD monolayer consists of three atomic layers, in which a transition-metal layer is sandwiched between two chalcogen layers.[10] Compared with their native 2D forms, zero-dimensional (0D) TMD quantum dots (QDs) with lateral sizes less than 10 nm show improved or new properties because of prominent edge and quantum confinement effects, such as larger surface-to-volume ratio, higher tunability in physiochemical properties, and more ease to be doped and functionalized.[11−16] For example, when a 2D MoS_2 nanosheet shrinks to 0D QD, it becomes photoluminescent.[17]

The study of chirality is one of the most intriguing research topics in many fields including biology, chemistry, pharmacy, and nanotechnology. In the area of nanotechnology, chirality of inorganic nanomaterials is an emerging and hot topic in the past several years. The chiral inorganic nanomaterials have shown potential applications in the areas such as sensing, cytotoxicity mediation and cell imaging, asymmetric catalysis and enantiomeric separation, circular polarized light emitting devices, and spintronics.[18] Among the chiral inorganic nanomaterials, considerable progress has been made on the preparation and application of chiral QDs including chiral semiconductor QDs[19−24] (i.e., CdSe QDs, CdS QDs) and chiral graphene QDs.[25] The typical method for the preparation of chiral QDs with optical activity is post-synthetic covalent modification of achiral QDs with chiral organic ligands to induce and control chirality.[26,27] Most recently, induced chirality was also found from 2D MoS_2 nanosheets by the modification of several chiral ligands.[18] According to the result, the origin of chirality in 2D MoS_2 nanosheets was related to the presence of chiral ligands causing preferential folding of the MoS_2 sheets.[28] Nevertheless, to best of our knowledge, there is no study for preparing 0D TMD-based chiral QDs. Obviously, folding and other kinds of deformation in 0D TMD QDs should be negligible. However, comparing the 2D nanosheets with large lateral area, TMD QDs possess some unique properties such as photoluminescence (PL),[29] easier cellular uptake,[17] enhanced quantum confinement, and edge effects resulting larger band gap.[30] Therefore, preparation and characterization of chiral TMD QDs is highly demanding in

Received: June 25, 2018
Accepted: August 16, 2018
Published: August 16, 2018

DOI: 10.1021/acsami.8b10594
ACS Appl. Mater. Interfaces 2018, 10, 30680−30688

relevant areas of science and technology such as chiral sensor, biomedical imaging, and nanomedicine.

Over the past decade, nanoenzymes which aimed to imitate the essential of natural enzymes have been reported by using versatile nanomaterials, such as Fe_3O_4 nanoparticles,[31] carbon nanotube,[32] and ruthenium nanoparticles.[33] In comparison with natural enzymes, nanomaterial-based artificial enzymes have the advantages of low costs, tuneable catalytic activities, high stability, and resistant to the changes of environmental conditions.[34] All these nanozymes turned out to have excellent enzyme-like catalytic activity but mostly do not possess enantioselectivity which is one of the most intrinsic properties of natural enzymes. Although exceedingly few examples of nanozymes reported with moderate enantioselectivity,[35,36] a potent enantioselective nanozyme is still urgently required. Interestingly, the MoS_2 nanoflowers[37] and MoS_2 nanosheets[38] were reported to possess peroxidase-like activity. Inspired by this, we anticipate that a chiral TMD QDs may be a more realistic mimetic enzyme with enantioselectivity.

Herein, we demonstrate the preparation of several kinds of chiral TMD QDs (MoS_2 and WS_2 QDs) by a direct sonication treatment of bulk TMDs and subsequent a covalent modification with chiral thiol ligands, that is, cysteine (Cys) and penicillamine (Pen). The chiral TMD QDs have been characterized by UV−vis absorption spectroscopy, PL spectroscopy, circular dichroism (CD) spectroscopy, and other spectroscopic and microscopic techniques. In addition, we have also found that the chiral TMD QDs displayed enantioselective peroxidase activity with the assistance of copper ions (Cu^{2+}) by using D- and L-tyrosinol (Tyr) enantiomers as the model substrates. Our study should be the first to prepare chiral TMD QDs and find out their enantioselective catalysis. We have also explored and verified enantioselective mechanism by using the quartz crystal microbalance (QCM) technique.

2. EXPERIMENTAL SECTION

2.1. Materials and Reagents. *N*-Methyl-2-pyrrolidone (NMP, 99.5%, anhydrous), sodium hydroxide (NaOH), and copper dichloride ($CuCl_2$) were purchased from Kelong Chemical Co. Ltd. (Chengdu, China). Bulk MoS_2 powder, WS_2 powder, L-Cys, D-Pen, L-Tyr, and 3,3′,5,5′-tetramethylbenzidine (TMB) were obtained from Aladdin Chemistry Co., Ltd. (Shanghai, China). D-Cys was obtained from Macklin Biochemical Technology Co., Ltd. (Shanghai, China). L-Pen was purchased from J&K Scientific Ltd. (Beijing, China). D-Tyr was purchased from Aldrich Chemical Co., Inc. (Milwaukee, USA). All reagents were of analytical grade and used without further purification. The water used throughout all experiments was deionized water purified through a Millipore system.

2.2. Instrumentation. Sonication exfoliation process of bulk TMD powder was carried out using a BRANSON S-250D ultrasonic disintegrator. Transmission electron microscopy (TEM) and high-resolution TEM (HRTEM) were performed by using a Tecnai G2 F20 S-TWIN TEM. UV−vis absorption spectra were obtained using an Agilent Cary 60 spectrometer. The Shimadzu RF-5301PC fluorospectrophotometer was used to record the PL properties of TMD QDs. The chiroptical activity of the TMD QDs was measured by Applied Photophysics CHIRASCAN CD spectrometer in aqueous solution. Fourier transform infrared (FT-IR) spectroscopy spectra were acquired with a Bruker TENSOR27 instrument. The QCM experiments were performed on the QCM200 (Stanford Research System). Surface charges of the QDs were evaluated with a Malvern Nano Zetasizer instrument. For surface charge measurements, the pH of a QDs suspension in water solution was at 7.0.

2.3. Preparation of TMD QDs. Both MoS_2 and WS_2 QDs were prepared by a direct sonication treatment with NaOH in NMP solution.[39] Typically, MoS_2 or WS_2 raw powders (0.35 g) were dispersed in 30 mL NMP solution followed by sonication for 3 h at the power of 200 W in ice-bath. Then 2 mL NaOH water solution (0.5 M) was added into solution followed by sonication for another 2 h under the same conditions. Subsequently, the sample was centrifuged for 10 min at 8000 rpm. The precipitate was discarded, whereas the supernatant was redispersed in NMP solution. Then, the resultant dispersion solution was filtered several times through a polytetrafluoroethylene microporous membrane with pore size of 0.2 μm. Eventually, the solution was dialyzed in a 500 Da dialysis bag against water for 4 d to remove excess NMP and salt. The resultant solution was freeze-dried, and a powder of TMD QDs was obtained. The as-prepared TMD QDs were redispersed in water for further use.

2.4. Preparation of Chiral TMD QDs. The synthesis of chiral TMD QDs was carried out at room temperature using D-Cys (or L-Cys, D- or L-Pen). Briefly, 4 mg of TMD QDs was resolved in 20 mL water solution. In a round-bottom flask, 1 mmol of D-Cys (or L-Cys, D- or L-Pen) was dissolved in 15 mL water, followed by adjusting the pH value to 11.2 with 0.5 M NaOH. Then, the chiral ligand solution was added to the flask containing TMD QDs solution, and the mixture was stirred intensely for 24 h. Subsequently, excess chiral ligands were removed by dialysis in a 500 Da dialysis bag in water for 7 d. Finally, the resultant solution was freeze-dried, and a powder of chiral TMD QDs was obtained. The prepared MoS_2 (or WS_2) QDs functionalized with D-Cys (or L-Cys, D- or L-Pen) were recorded as D-Cys (or L-Cys, D- or L-Pen)-MoS_2 (or WS_2) QDs for further use.

2.5. Preparation of D- and L-Cys-MoS_2 QDs/Cu^{2+}. D-Cys−MoS_2 QDs/Cu^{2+} were prepared by mixing D-Cys−MoS_2 QDs and $CuCl_2$ under sonication conditions. Briefly, 5 mL of aqueous solution containing 0.5 mg of D-Cys−MoS_2 QDs was under sonication for 10 min. Subsequently, 5 mL of $CuCl_2$ (0.1 M) was added into the above solution and stood overnight. The mix solution was removed in an ultrafiltration centrifuge tube (3 kD, Millipore) and centrifuged three times (8000 rpm, 20 min) to remove the unreacted copper. The residual solution was freeze-dried for further use. The same method was used to prepare L-Cys−MoS_2 QDs/Cu^{2+} conjugate.

2.6. Peroxidase-like Catalytic Activity Experiments. D- and L-Cys−MoS_2 QDs/Cu^{2+} were chosen to investigate the peroxidase-like activity of chiral TMD QDs. Peroxidase substrate TMB was selected for verifying the enzymatic-like activity of the chiral QDs. The experiments were carried out using 0.05 mg/mL D- or L-Cys−MoS_2 QDs/Cu^{2+} with a final reaction volume of 0.4 mL. The TMB concentration was 1 mM and H_2O_2 concentration was 10 mM. The effects of pH, temperature, and H_2O_2 concentration on the D- or L-Cys−MoS_2 QDs/Cu^{2+} peroxidase-like activity were examined in a mixture of 10 mM Tris-HCl buffer solution. The pH values from 3.23 to 9.14 were modulated by mixing different volumes of 10 mM Tris and 0.5 mM HCl solutions. The D- or L-Cys−MoS_2 QDs/Cu^{2+}−H_2O_2−TMB system was incubated in water baths at different temperature from 25 to 55 °C to determine the temperature-dependent catalytic activity. The chiral QDs/Cu^{2+} were incubated with different concentrations of H_2O_2 in the range from 0 to 80 mM at 25 °C to determine their H_2O_2 concentration-related catalytic activity (pH = 6.02).

To investigate the apparent kinetic parameters, the kinetic assays were carried out under standard reaction conditions at 25 °C in 1 cm thick quartz cuvette containing 0.4 mL of Tris-HCl buffer solution (pH = 6.02, 10 mM). The reactions were monitored in the time-drive mode at 652 nm on the UV−vis spectrophotometer. The steady-state kinetic analysis of L-Cys−MoS_2 QDs/Cu^{2+} (50 mg/mL) was performed by varying concentrations of TMB with a fixed concentration of H_2O_2 or vice versa. The kinetic parameters were obtained by the plot linear-fitting method based on the Lineweaver−Burk double-reciprocal equation derived from the Michaelis−Menten equation.

2.7. Enantioselectivity Investigations. For enantioselectivity assays of different concentrations of the chiral substrates D- and L-Tyr and D- and L-Cys−MoS_2 QDs/Cu^{2+} were tested in a concentration of 0.1 mg/mL. The H_2O_2 oxidation reactions were carried out using 1 mM D- or L-Tyr in a mixture of 10 mM Tris-HCl buffer solution. The

DOI: 10.1021/acsami.8b10594
ACS Appl. Mater. Interfaces 2018, 10, 30680−30688

pH values from 2.05 to 9.09 were modulated by mixing different volumes of 10 mM Tris and 0.5 mM HCl solutions. The D- or L-Cys−MoS_2 QDs/Cu^{2+}−H_2O_2−Tyr system was incubated in water baths at different temperature from 25 to 50 °C to determine the temperature-dependent catalytic activity. The D- or L-Cys−MoS_2 QDs/Cu^{2+} were incubated with different concentrations of H_2O_2 in the range from 0 to 80 mM at 30 °C to determine their H_2O_2 concentration-related catalytic activity. All time course assays were carried out by monitoring the absorbance change at 210 nm. The apparent kinetic parameters were calculated based on the function of Lineweaver−Burk double-reciprocal equation mentioned above.

2.8. QCM Experiments. The quartz sensor crystals used consist of an AT-cut quartz crystal of 14 mm of diameter and thickness 0.3 mm coated with Au. D- or L-Cys−MoS_2 QDs solution (1 mg/mL) was added dropwise on the quartz crystal to directly adsorb onto the bare sensor. The crystal stood 2 days until the sensor was saturated with the coating QDs completely. Then, the crystal was washed in water softly to remove without adhesion QDs. To set the baseline, the water was introduced using a peristaltic pump at the flow rate of 50 μL/min. The crystal was excited to oscillate at its characteristic fundamental frequency f_0 = 5 MHz. The 5 mM D- or L-Tyr solution was introduced in the system at the same flow rate and changes in frequency was recorded with time until steady.

3. RESULTS AND DISCUSSION

TMD QDs were prepared by a direct sonication treatment of bulk MoS_2 powder with NaOH in NMP solution (Scheme 1).[39] The TEM measurements were first used for character-

Scheme 1. Schematic Illustration for the Sonication Combined with Ion Intercalation Method in the Alkaline Environment for Preparation of TMD QDs, and the Covalent Modification with Chiral Ligands for Preparing Chiroactive TMD QDs[a]

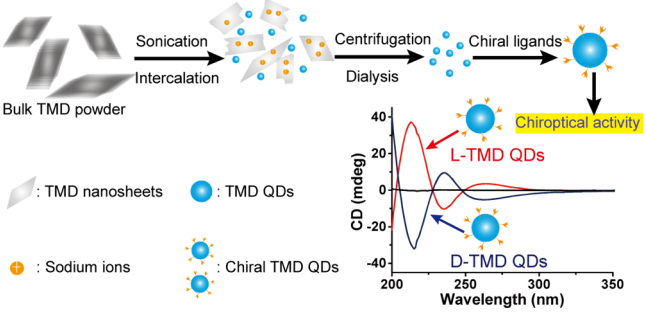

[a]Typical CD spectra of the chiral TMD QDs are shown in the scheme.

ization of structure and morphology of all of the TMD QDs. Figure 1A presented the typical TEM image of MoS_2 QDs, exhibiting a relatively uniform size distribution and well monodispersion and the average diameter of 2.03 ± 0.48 nm (Figure 1B). The HRTEM image (Figure 1C) demonstrated the crystallinity of the MoS_2 QDs, with a lattice parameter of 0.25 nm, which corresponded to the (103) plane of the bulk MoS_2 crystal.[40] Similarly, WS_2 QDs prepared by the same method were observed in the TEM image (Figure 1D), and the average size was about 2.00 ± 0.59 nm (Figure 1E). The highly crystalline structure of the WS_2 QDs was visualized in the HRTEM image (Figure 1F) and the lattice fringe spacing was about 0.27 nm, which was in agreement with the lattice spacing in (100) direction of WS_2.[41] The monodispersion state of both MoS_2 QDs and WS_2 QDs after chiral modification was kept unchanged (Figure S1). To make the results more convincible,

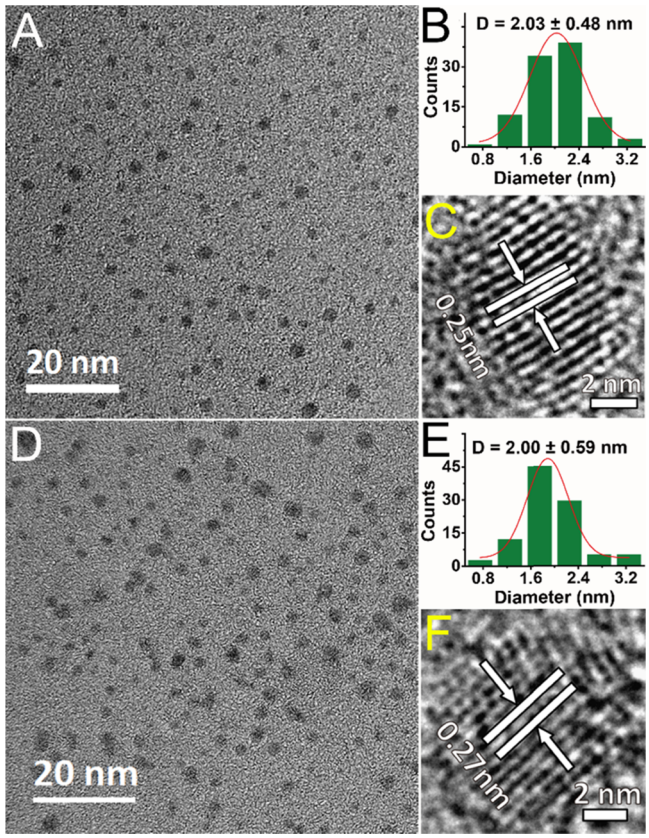

Figure 1. (A) TEM image of MoS_2 QDs. (B) Size distribution of MoS_2 QDs. (C) HRTEM image of MoS_2 QDs. (D) TEM image of WS_2 QDs. (E) Size distribution of WS_2 QDs. (F) HRTEM image of WS_2 QDs.

the crystal structure of both MoS_2 QDs and WS_2 QDs was investigated through X-ray diffraction (XRD) with bulk MoS_2 and WS_2 as the references (Figure S2). Compared with bulk MoS_2, the (002) diffraction peak at 2θ = 14.4 disappears in the MoS_2 QDs, which is attributed to the thin-layer structure of the QDs. The (100) or (101) diffraction peak at 2θ = 32.8 is retained in the MoS_2 QDs.[42] Similar XRD results were obtained for WS_2 QDs. Raman spectroscopy was further utilized to characterize the crystal structure of MoS_2 QDs and WS_2 QDs (Figure S3). Take MoS_2 QDs for example, two strong Raman peaks could be observed at 377.4 and 404.4 cm^{-1} for bulk MoS_2, which were assigned to in-plane ($^1E_{2g}$) and vertical plane (A_{1g}) vibration of Mo−S bonds in MoS_2, respectively. The corresponding bands for MoS_2 QDs were located at 379.0 and 402.3 cm^{-1}. It was obvious that the MoS_2 QDs had a smaller Raman shift difference between $^1E_{2g}$ and A_{1g} modes compared with the bulk counterpart, which was attributed to the $^1E_{2g}$ stiffening and A_{1g} softening with decreasing layer thickness and lateral size.[43] Characteristic Raman bands with slight shifting were observed for WS_2 QDs as well (Figure S3B). All of the above results confirmed that the nanoparticles were indeed MoS_2 QDs and WS_2 QDs.

Starting from MoS_2 QDs, we explored the chemical composition with X-ray photoelectron spectroscopy (XPS) measurements. Compared with bulk MoS_2 crystal, XPS spectra of MoS_2 QDs indicated that a little amount of Mo was oxidized from Mo^{4+} to Mo^{6+} during the preparation of MoS_2 QDs (Figure S4). According to the XPS analysis, the molar ratio of Mo^{4+} to Mo^{6+} was about 8.63:1. Similarly, XPS measurements

DOI: 10.1021/acsami.8b10594
ACS Appl. Mater. Interfaces 2018, 10, 30680−30688

indicated that the W was also partially oxidized in the WS_2 QDs (Figure S5). The molar ratio of W^{4+} to W^{6+} was about 2.63:1. The oxidization of the metal elements would be avoided by preparing TMD QDs under nitrogen protection.

The optical properties of TMD QDs were then studied by using fluorescence and UV−vis absorption spectroscopy. As the excitation wavelength ranged from 350 to 450 nm, the PL peak of MoS_2 QDs shifted to longer wavelength from 436 to 529 nm (Figure 2A). In addition, another PL study was carried

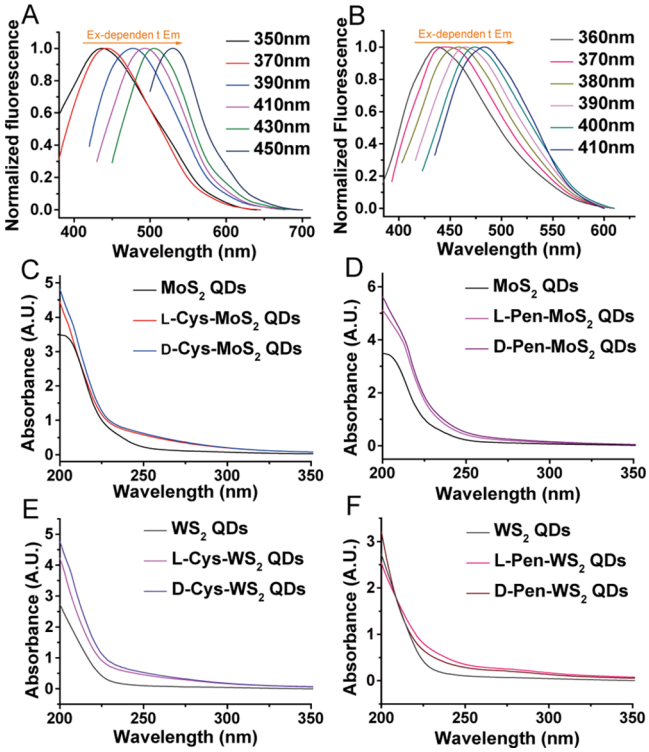

Figure 2. PL spectra of (A) MoS_2 QDs, and (B) WS_2 QDs by various wavelength excitations ranging from 350 to 450 nm. (C) UV−vis spectra of MoS_2 QDs, D- and L-Cys−MoS_2 QDs. (D) UV−vis spectra of MoS_2 QDs, D- and L-Pen−MoS_2 QDs. (E) UV−vis spectra of WS_2 QDs, D- and L-Cys−WS_2 QDs. (F) UV−vis spectra of WS_2 QDs, D- and L-Pen−WS_2 QDs.

out by analyzing WS_2 QDs (Figure 2B) at excitation wavelengths ranging from 360 to 410 nm. It could be seen that the emission peak showed a red shift (from 437 to 484 nm) as the excitation shifted toward longer wavelengths. According to the PL spectra, TMD QDs exhibited excitation-dependent PL behavior,[44] which had been widely reported, such as in carbon dots,[45] GQDs,[46] and CdSe nanorods.[47] These observations suggested that the excitation-dependent PL behavior might be attributed to the polydispersity or the surface state of QDs.[48] All of the prepared chiral TMD QDs showed similar excitation-dependent emission properties.

Then, the chiral TMD QDs were further characterized. All chiral TMD QDs can solubilize in water forming transparent light-yellow solutions (Figure S6A). The chiral TMD QDs solutions emitted bright blue light under UV illumination (Figure S6B). To explore the optical properties of TMD QDs, the UV−vis absorption spectra of chiral Cys−MoS_2 QDs and chiral Pen−MoS_2 QDs are presented in Figure 2C,D, which demonstrated similar optical absorption region of bare MoS_2 QDs from 300 to 200 nm. Figure 2E,F shows UV−vis spectra of chiral Cys−WS_2 QDs, chiral Pen−WS_2 QDs and their unmodified WS_2 QDs. The optical absorption features in the UV region (200−300 nm) with a tail extending into the visible range had similarities because of the excitonic features.[49]

FT-IR spectra of the chiral TMD QDs are presented in Figure S7. The FT-IR spectra of the chiral ligand enantiomers are shown in Figure S7A,B. L-Cys molecule showed the characteristic vibrations of the N−H bending at 1532 cm^{-1} and the asymmetric and symmetric stretching of COO^- at 1600 and 1390 cm^{-1}.[50] However, after the functionalization of L- or D-Cys onto the surface of TMD QDs, slight changes in the above wavenumbers were observed in the spectra of D- and L-Cys−MoS_2 QDs (Figure S7C) and D- and L-Cys-WS_2 QDs (Figure S7E). Shifts in the position of characteristic vibrations were likely due to changes in their dipole moment when Cys molecules bound on TMD QDs surface with high electron density.[51] Significantly, the weak band at 2550 cm^{-1} because of the presence of the S−H band[52] was not observed in the spectra of the Cys-capped QDs, implying the formation of the covalent bond between Cys ligand and TMD QDs. The similar results were also detected in the Pen-modified QDs (Figure S7D,F).

The elemental composition of the chiral TMD QDs was analyzed by XPS measurements. Take L-Cys−MoS_2 QDs for example, the Mo 3d XPS spectra ranging from 222 to 240 eV was a little different to that of MoS_2 QDs. Possibly because of the reductive activity of the chiral ligand L-Cys, the content of Mo^{6+} was reduced (Figure S8). The S 2p was studied from the range of 160−172 eV, enabling the MoS_2 to be identified between 164 and 160 eV. Another broad peak was identified in the region from 164 to 170 eV and was assigned to the origin of the sulfur from L-Cys ligands present. Therefore, XPS results have enabled us to confirm the attachment of the ligand to the surface of the MoS_2 and in addition allowed us to confirm the chemical nature of the QDs as MoS_2.[28] Because the QDs are thin-layers, the molar ratio of the elements (Mo/S/N) in L-Cys−MoS_2 QDs was calculated to be 1:2.48:0.52 according to Mo 3d, S 2p, and N 1s peak areas using the empirical atomic sensitivity factors for them.[53] Obviously, the N atoms came from the chiral ligand L-Cys with 1:1 stoichiometry. Therefore, the weight content of L-Cys in L-Cys−MoS_2 QDs solid was ca. 28%. The composition of chiral WS_2 was also surveyed by XPS (Figure S9).

The chiroptical activity of the QDs was then investigated. The CD spectra of the chiral ligand enantiomers are shown in Figure 3A,B. The D- and L-Cys−MoS_2 QDs resulted in CD spectra of crossing zero and opposite signs as the Cotton effect in chiroptical activity (Figure 3C).[54] They were distinct to those of D- and L-Cys. Importantly, each CD curves of D- and L-Cys−MoS_2 QDs had bands at 212 and 265 nm of opposite sign, which were classical bisignated line shape (so-called exciton couplet)[55] indicating that the Cotton effects were not dispersive phenomena but due to preferential excitation of the split bands by alternating circular polarizations.[56] Similarly, D- and L-Pen could also lead to induced chirality in QDs. As shown in Figure 3D, it was evident that the first absorption peak coincided with the CD peak for corresponding D- and L-Pen, and new bands at 235 and 264 nm with opposite sign exhibited similar bisignated features, and also proved additional chiroactivity were induced in D- and L-Pen−MoS_2 QDs.

The chiral ligand molecules induced a chiroptical response in the inorganic TMD QDs' exciton transitions as a result of an electronic interaction, which could be summarized as a simple

DOI: 10.1021/acsami.8b10594
ACS Appl. Mater. Interfaces 2018, 10, 30680−30688

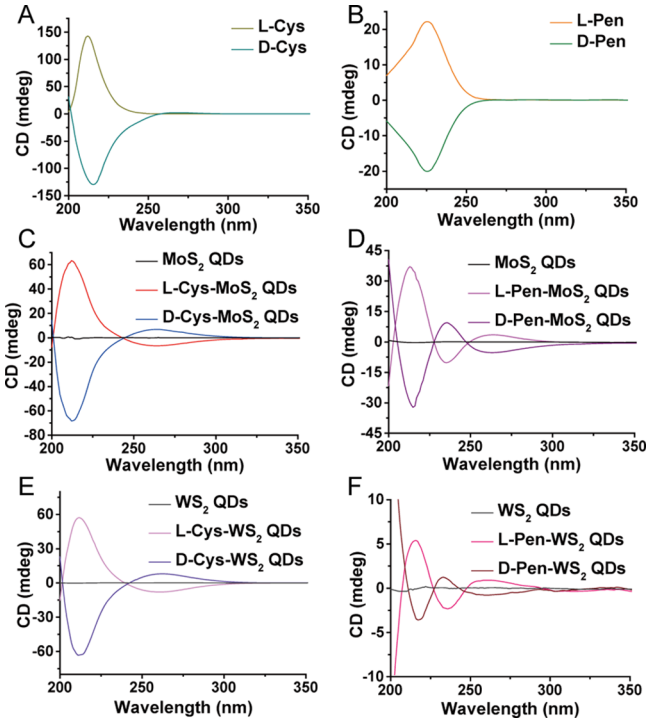

Figure 3. CD spectra of (A) L-Cys and D-Cys, (B) L-Pen and D-Pen, (C) MoS_2 QDs, D- and L-Cys−MoS_2 QDs, (D) MoS_2 QDs, D- and L-Pen−MoS_2 QDs, (E) WS_2 QDs, D- and L-Cys−WS_2 QDs, and (F) WS_2 QDs, D- and L-Pen−WS_2 QDs.

dipolar interaction between the excitations of QDs and of ligand molecules.[57] Furthermore, induced chiroptical properties can be assigned to the different excitonic transitions and each transition was accompanied by a derivative line shape in the CD response, indicating that the chiral ligand can split the exciton level into two new sublevels.[56] The CD induction mechanism primarily acts on an electronic interaction effect between the adsorbed chiral molecules levels and the electron hole states of QD's levels.[19,58] In addition, this result was also similar to that of D- and L-Cys or D- and L-Pen stabilized WS_2 QDs (Figure 3E,F).

To make our chiral TMD QDs more useful, we further explored their chiral selectivity and potential applicability. Inspired by peroxidase-like activity of the MoS_2 nanoflowers[37] and MoS_2 nanosheets,[38] we tried to investigate whether the chiral TMD QDs had peroxidase-like activity as well. The classic peroxidase substrate TMB was used for this purpose. Generally, peroxidase and peroxidase-like mimetics can catalyze the oxidation of colorless TMB to colored oxidized products which shows absorbance peaks at 369 and 652 nm.[59] Taking the chiral D- and L-Cys−MoS_2 QDs as the examples, we evaluated their peroxidase activity and enantioselectivity. As shown in Figure 4A, unmodified MoS_2 QDs cannot catalyze the oxidation of TMB within 10 min in the presence of H_2O_2. After adding with H_2O_2 in the TMB solution, unmodified MoS_2 QDs showed no peroxidase-like activity (Figure 4A) indicating the as-prepared MoS_2 QDs do not possess peroxidase-like activity. Similarly, both D- and L-Cys−MoS_2 QDs showed negligible peroxidase activity either. In respect of this, we tried to seek a cofactor to enhance the catalytic activity of the chiral QDs. Interestingly, Cu^{2+} is commonly found as the active sites in natural enzymes such as heme/copper oxidases[60] and laccase,[61] and it is often chosen as the element

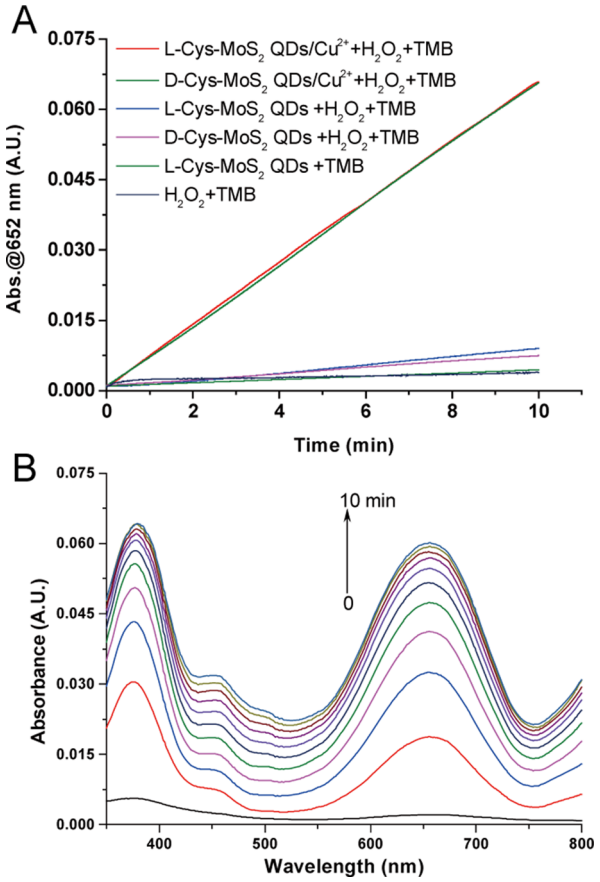

Figure 4. (A) Time-dependent absorbance changes at 652 nm of TMB solution in different reaction systems. (B) UV−vis spectra change in the system of L-Cys−MoS_2 QDs/Cu^{2+} + H_2O_2 + TMB within 10 min. The concentration of L-Cys−MoS_2 QDs/Cu^{2+}, TMB, and H_2O_2 are 50 mg/mL, 1 mM, 10 mM, respectively.

for the design and synthesis of artificial enzymes.[62] For example, Cu^{2+} endowed carbon nitride nanoparticles and carbon dots horseradish peroxidase-like biocatalytic functions.[63] Inspired by this, we investigated the effect of Cu^{2+} as a cofactor for D- or L-Cys−MoS_2 QDs. The preparation of D- or L-Cys−MoS_2 QDs/Cu^{2+} conjugates was shown in Experimental Section, and both of them displayed well monodispersion as indicated by TEM images (Figure S10). The zeta potential of D- or L-Cys−MoS_2 QDs was measured to be −8.3 and −9.1 mV; and after association with Cu^{2+}, their zeta potential changed to be +25.2 and +27.8 mV, respectively. The zeta potential measurements further confirmed the formation of D- or L-Cys−MoS_2 QDs/Cu^{2+} conjugates. Furthermore, the CD spectra showed that chirality of D- or L-Cys−MoS_2 QDs was retained with the conjugation of Cu^{2+} (Figure S11). Inductively coupled plasma optical emission spectroscopy (ICP-OES) indicates a coverage of Cu^{2+} corresponding to 0.102 mg per milligram of D- or L-Cys−MoS_2 QDs/Cu^{2+} conjugates. Fortunately, with the assistance of Cu^{2+}, the D- and L-Cys−MoS_2 QDs both exhibited highly peroxidase-like activities to the achiral substrate TMB (Figure 4A). Figure 4B shows the typical UV−vis absorption spectra change in the system of L-Cys−MoS_2 QDs/Cu^{2+} for oxidizing TMB within 10 min. Control experiments (Figure S12) indicate that Cu^{2+} (in the form of $CuCl_2$) at the same content associated with the D- or L-Cys−MoS_2 QDs/Cu^{2+} conjugates do not reveal any catalytic properties toward the oxidization of TMB. Thus, the

DOI: 10.1021/acsami.8b10594
ACS Appl. Mater. Interfaces 2018, 10, 30680−30688

peroxidase-like activity is not an intrinsic property of Cu^{2+} but originates from the conjugates. The catalytic behavior of D- or L-Cys−MoS_2 QDs/Cu^{2+} conjugates was similar to natural enzyme, which was dependent on pH, temperature, and H_2O_2 concentration (Figure S13). Under our experimental conditions, the optimal pH, temperature, and H_2O_2 concentration were 6.02, 25 °C, and 40 mM, respectively.

The steady-state kinetics of D- or L-Cys−MoS_2 QDs/Cu^{2+} conjugates was investigated by the Michaelis−Menten curve by keeping the concentration of TMB or H_2O_2 constant and changing the concentration of the other (Figure S14). According to Lineweaver−Burk equation[64] and calculation of a series of steady-state reaction rates (Figure S14C,D), the Michaelis−Menten constant (K_m) and the maximum initial velocity (V_{max}) are listed in Table S1. All of the results indicated that both D- and L-Cys−MoS_2 QDs/Cu^{2+} conjugates followed the typical Michaelis−Menten behavior[65] toward interacting with TMB and H_2O_2. The results further confirmed that D- and L-Cys−MoS_2 QDs/Cu^{2+} conjugates possess the peroxidase-like activity. In theory, the surface of D- and L-Cys−MoS_2 QDs has plenty of carboxylic and amino groups which can bind Cu^{2+} with high affinity to form stable conjugate and consequently exhibit catalytic activity alike the previously reported carbon nitride nanoparticles and carbon dots did.[63] Interestingly, the catalyst (i.e., L-Cys−MoS_2 QDs/Cu^{2+}) was recyclable with centrifugation- and sonication-assisted redispersion. The V_{max} of L-Cys−MoS_2 QDs/Cu^{2+} toward the substrate TMB was kept almost unchanged after being recycled three times, and it was gradually decreased after being recycled five times (Figure S15). The results indicated that the catalyst is beneficial to be recyclable. The decreased catalysis ability after 10 times recycling was experimentally investigated. According to dynamic light scattering and ICP-OES measurements, the decreased catalytic activity should be due to partial aggregation and loss of Cu^{2+} of the L-Cys−MoS_2 QDs/Cu^{2+} conjugates.

We subsequently evaluate the enantioselective peroxidase-like activity of D- and L-Cys−MoS_2 QDs/Cu^{2+} conjugates toward D- and L-Tyr enantiomers. The oxidation product of Tyr could be detected by monitoring the absorbance change at 210 nm (Figure S16). The time-dependent absorbance change assays showed that no oxidation of Tyr occurred by Cu^{2+} alone or weakly oxidation of Tyr by unmodified MoS_2 QDs plus Cu^{2+} (Figure 5). Obviously, both D- and L-Cys−MoS_2 QDs/Cu^{2+} could lead to chiral selective oxidation of D- and L-Tyr enantiomers. Therein, D-Cys−MoS_2 QDs/Cu^{2+} showed much higher catalytic activity than L-Cys−MoS_2 QDs/Cu^{2+} (Figure 5A) to catalyze the oxidation of D-Tyr. As expected, the L-Cys−MoS_2 QDs/Cu^{2+} showed much higher catalytic activity than D-Cys−MoS_2 QDs/Cu^{2+} to catalyze the oxidation of L-Tyr (Figure 5B).

The enantioselective steady-state kinetics of D- and L-Cys−MoS_2 QDs/Cu^{2+} conjugates toward chiral substances were further measured. They also showed pH, temperature, and H_2O_2 concentration-dependent catalytic activities (Figure S17). According to Figures S18 and S19, K_m and V_{max} of D- and L-Cys-MoS_2 QDs/Cu^{2+} were obtained using Lineweaver−Burk plot and are shown in Table 1. With regard to L-Cys−MoS_2 QDs/Cu^{2+}, the values of K_m for L- and D-Tyr were 9.96×10^{-4} and 6.61×10^{-3} M, respectively, indicating that L-Cys−MoS_2 QDs/Cu^{2+} displayed higher binding affinity to L-Tyr than D-Tyr. Oppositely, K_m values of D-Cys−MoS_2 QDs/Cu^{2+} toward L- and D-Tyr were 5.46×10^{-3} and 8.06×10^{-4} M,

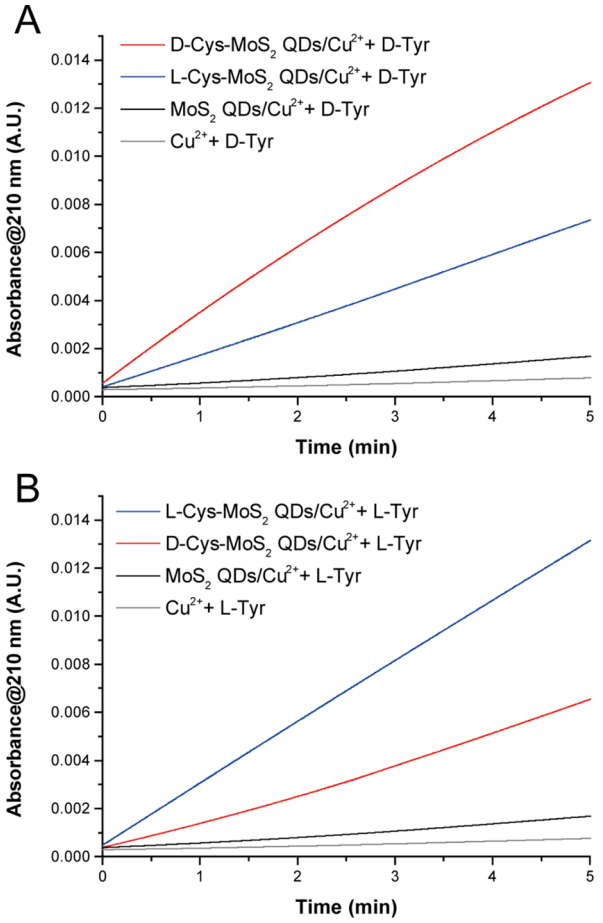

Figure 5. Time-dependent absorbance changes of (A) D-Tyr and (B) L-Tyr in the presence of L-Cys−MoS_2 QDs/Cu^{2+}, D-Cys−MoS_2 QDs/Cu^{2+}, MoS_2 QDs/Cu^{2+}, and Cu^{2+} system with H_2O_2 at 210 nm. The concentration of D- or L-Cys−MoS_2 QDs/Cu^{2+}, D- or L-Tyr, and H_2O_2 are 0.1 mg/mL, 1 mM, and 10 mM, respectively.

Table 1. Michaelis−Menten Constant (K_m) and Maximum Reaction Rate (V_{max}) of L- and D-Cys-MoS_2 QDs/Cu^{2+} Conjugates Toward L- and D-Tyr

catalysts	substrates	K_m (M)	V_{max} ($M \cdot s^{-1}$)
L-Cys−MoS_2 QDs/Cu^{2+}	L-Tyr	9.96×10^{-4}	5.08×10^{-7}
L-Cys−MoS_2 QDs/Cu^{2+}	D-Tyr	6.61×10^{-3}	1.97×10^{-7}
D-Cys−MoS_2 QDs/Cu^{2+}	L-Tyr	5.46×10^{-3}	1.83×10^{-7}
D-Cys−MoS_2 QDs/Cu^{2+}	D-Tyr	8.06×10^{-4}	4.95×10^{-7}

respectively. Thus, the enantioselectivity ratio of K_m value toward L- and D-Tyr are 0.145 and 6.77 (6.77 multiply by 0.145 approximately equals to 1) for L- and D-Cys−MoS_2 QDs/Cu^{2+} conjugates, respectively. Significantly, the enantioselectivity reported herein is much better than that of recently reported chiral nanozymes,[37,38] in which the enantioselectivity is only slightly higher than 1. Furthermore, the D- and L-Cys−MoS_2 QDs/Cu^{2+} conjugates showed opposite enantioselectivity, which were in good accordance with the first principle of stereochemistry,[66] and indicated the robustness of our results. Even more noteworthy is the on-demand reversibility of enantioselectivity of our chiral TMD QDs, which show extraordinary advantages to natural enzymes because the stereoselectivity of a natural enzyme can be evoluted only by genetical engineering with unexpectable variation.

DOI: 10.1021/acsami.8b10594
ACS Appl. Mater. Interfaces 2018, 10, 30680−30688

For further understanding the mechanism of enantioselectivity, we make use of the QCM technique to monitor the interaction differences between chiral Cys−MoS_2 QDs/Cu^{2+} conjugates and Tyr substrates. Figure 6A shows the frequency

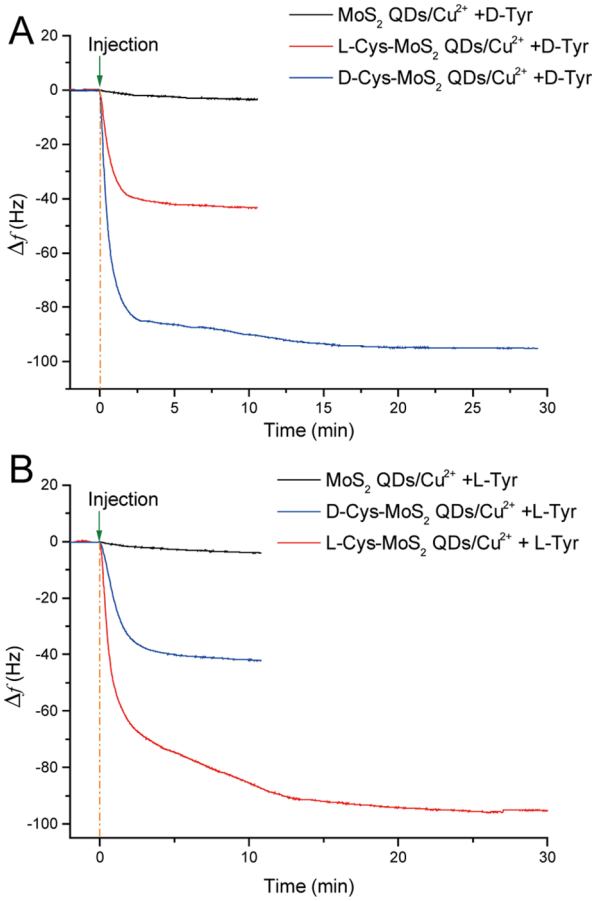

Figure 6. Frequency shifts of the D- and L-Cys−MoS_2 QDs/Cu^{2+}-immobilized QCM sensor exposed to (A) 5 mM D-Tyr and (B) 5 mM L-Tyr solution.

shift (Δf) observed when solutions of D-Tyr flowed over the D- or L-Cys−MoS_2 QDs/Cu^{2+} conjugate-immobilized QCM chip, giving a clear difference. In addition, control experiment using unmodified MoS_2 QDs/Cu^{2+} immobilized onto the quartz chip gave frequency shifts both below 5 Hz ruling out interferences from nonspecific surface absorption of D- or L-Tyr. In the standard interpretation of QCM analysis, Δf is proportional to the adsorption affinity between the crystal surface and analyte.[67] That is, the D-Cys−MoS_2 QDs/Cu^{2+} conjugate interacted stronger with D-Tyr than L-Tyr. In comparison, the binding capability of the L-Cys−MoS_2 QDs/Cu^{2+} conjugate was almost completely opposite to D-Cys−MoS_2 QDs/Cu^{2+} (Figure 6B), further indicating the robustness of our results. According to the principle of natural enzymes and previously reported nanozymes, lower and previously reported nanozymes, lower K_m value indicated a higher affinity between the enzymes to the substrates.[68] Herein, the QCM results were in good accordance with K_m values and are listed in Table 1. We deduced that the enantioselective peroxidase-like catalysis of the TMD QDs/Cu^{2+} conjugates should be due to the formation of chiral Cu^{2+} complexes on the QDs surface. A more detailed mechanism of the affinity between chiral QDs/Cu^{2+} conjugates and Tyr enantiomers is still being studied, and our work is the first to show that chiral TMD QDs can act as nanozyme with enantioselectivity.

4. CONCLUSIONS

In summary, the TMD QDs were prepared through a facile, universal top-down sonication process and we had developed an approach for the production of chiral TMD QDs (MoS_2 and WS_2 QDs) by a covalent modification process with chiral ligands (Cys and Pen). We used spectroscopic and microscopic techniques to investigate their optical properties and morphology characteristics. The D- and L-Cys-modified chiral TMD QDs revealed a 200−240 nm CD peak corresponding to the Cys enantiomers and displayed a new chiroptical band at 250−350 nm. For the D- and L-Pen-modified chiral TMD QDs, the original 200−260 nm CD peak corresponding to the Pen enantiomers was split into two CD peaks with opposite signs at 210−220 and 220−250 nm and displayed a new CD peak at 250−350 nm. Most interestingly, with the assistance of Cu^{2+}, the chiral QDs possess peroxidase-like activity and have enantioselectivity for catalysis oxidation chiral Tyr substrates owning to the differences of binding affinities between chiral QDs and Tyr substrates. These results showed that the chiral TMD QDs had great potential in applying as enantioselective catalyst and our work is in favor of inspiring better design of chiral nanozymes.

■ ASSOCIATED CONTENT

Supporting Information

The Supporting Information is available free of charge on the ACS Publications website at DOI: 10.1021/acsami.8b10594.

FT-IR, TEM, and some UV−vis spectra-based data (PDF)

■ AUTHOR INFORMATION

Corresponding Author

*E-mail: wlwei@cqu.edu.cn.

ORCID

Zhining Xia: 0000-0002-2064-5880

Weili Wei: 0000-0001-6363-3591

Author Contributions

The manuscript was written through contributions of all authors. All authors have given approval to the final version of the manuscript.

Notes

The authors declare no competing financial interest.

■ ACKNOWLEDGMENTS

This work was financially supported by the National Natural Science Foundation of China (no. 21675016), the Fundamental Research Funds for the Central Universities of China (no. 106112017CDJQJ238815), Chongqing Basic and Frontier Research Program (no. cstc2016jcyjA0328), and the 100 Young Plan by Chongqing University (no. 0236011104410).

■ REFERENCES

(1) Zhou, S.; Liu, N.; Wang, Z.; Zhao, J. Nitrogen-Doped Graphene on Transition Metal Substrates as Efficient Bifunctional Catalysts for Oxygen Reduction and Oxygen Evolution Reactions. *ACS Appl. Mater. Interfaces* **2017**, *9*, 22578−22587.

(2) Wei, W.; Qu, X. Extraordinary Physical Properties of Functionalized Graphene. *Small* **2012**, *8*, 2138−2151.

(3) Tan, C.; Cao, X.; Wu, X.-J.; He, Q.; Yang, J.; Zhang, X.; Chen, J.; Zhao, W.; Han, S.; Nam, G.-H.; Sindoro, M.; Zhang, H. Recent Advances in Ultrathin Two-Dimensional Nanomaterials. *Chem. Rev.* **2017**, *117*, 6225−6331.
(4) Zhang, X.; Cheng, H.; Zhang, H. Recent Progress in the Preparation, Assembly, Transformation, and Applications of Layer-Structured Nanodisks beyond Graphene. *Adv. Mater.* **2017**, *29*, 1701704.
(5) Shotan, Z.; Jayakumar, H.; Considine, C. R.; Mackoit, M.; Fedder, H.; Wrachtrup, J.; Alkauskas, A.; Doherty, M. W.; Menon, V. M.; Meriles, C. A. Photoinduced Modification of Single-Photon Emitters in Hexagonal Boron Nitride. *ACS Photonics* **2016**, *3*, 2490−2496.
(6) Jiang, G.; Zhou, C.-H.; Xia, X.; Yang, F.; Tong, D.; Yu, W.; Liu, S. Controllable Preparation of Graphitic Carbon Nitride Nanosheets via Confined Interlayer Nanospace of Layered Clays. *Mater. Lett.* **2010**, *64*, 2718−2721.
(7) Jeong, H. Y.; Lee, S. Y.; Ly, T. H.; Han, G. H.; Kim, H.; Nam, H.; Jiong, Z.; Shin, B. G.; Yun, S. J.; Kim, J.; Kim, U. J.; Hwang, S.; Lee, Y. H. Visualizing Point Defects in Transition-Metal Dichalcogenides Using Optical Microscopy. *ACS Nano* **2016**, *10*, 770−777.
(8) Chhowalla, M.; Shin, H. S.; Eda, G.; Li, L.-J.; Loh, K. P.; Zhang, H. The Chemistry of Two-Dimensional Layered Transition Metal Dichalcogenide Nanosheets. *Nat. Chem.* **2013**, *5*, 263−275.
(9) Tan, C.; Luo, Z.; Chaturvedi, A.; Cai, Y.; Du, Y.; Gong, Y.; Huang, Y.; Lai, Z.; Zhang, X.; Zheng, L.; Qi, X.; Goh, M. H.; Wang, J.; Han, S.; Wu, X.-J.; Gu, L.; Kloc, C.; Zhang, H. Preparation of High-Percentage 1T-Phase Transition Metal Dichalcogenide Nanodots for Electrochemical Hydrogen Evolution. *Adv. Mater.* **2018**, *30*, 1705509.
(10) Roldán, R.; Castellanos-Gomez, A.; Cappelluti, E.; Guinea, F. Strain Engineering in Semiconducting Two-Dimensional Crystals. *J. Phys.: Condens. Matter* **2015**, *27*, 313201.
(11) Wang, X.; Sun, G.; Li, N.; Chen, P. Quantum Dots Derived from Two-Dimensional Materials and Their Applications for Catalysis and Energy. *Chem. Soc. Rev.* **2016**, *45*, 2239−2262.
(12) Song, X.-X.; Liu, D.; Mosallanejad, V.; You, J.; Han, T.-Y.; Chen, D.-T.; Li, H.-O.; Cao, G.; Xiao, M.; Guo, G.-C.; Guo, G.-P. A gate defined quantum dot on the two-dimensional transition metal dichalcogenide semiconductor WSe_2. *Nanoscale* **2015**, *7*, 16867−16873.
(13) Chen, Z.; Tao, Z.; Cong, S.; Hou, J.; Zhang, D.; Geng, F.; Zhao, Z. Fast Preparation of Ultrafine Monolayered Transition-Metal Dichalcogenide Quantum Dots Using Electrochemical Shock for Explosive Detection. *Chem. Commun.* **2016**, *52*, 11442−11445.
(14) Lai, Z.; Chaturvedi, A.; Wang, Y.; Tran, T. H.; Liu, X.; Tan, C.; Luo, Z.; Chen, B.; Huang, Y.; Nam, G.-H.; Zhang, Z.; Chen, Y.; Hu, Z.; Li, B.; Xi, S.; Zhang, Q.; Zong, Y.; Gu, L.; Kloc, C.; Du, Y.; Zhang, H. Preparation of 1T′-Phase $ReS_{2x}Se_{2(1-x)}$ (x = 0-1) Nanodots for Highly Efficient Electrocatalytic Hydrogen Evolution Reaction. *J. Am. Chem. Soc.* **2018**, *140*, 8563−8568.
(15) Yu, Y.; Nam, G.-H.; He, Q.; Wu, X.-J.; Zhang, K.; Yang, Z.; Chen, J.; Ma, Q.; Zhao, M.; Liu, Z.; Ran, F.-R.; Wang, X.; Li, H.; Huang, X.; Li, B.; Xiong, Q.; Zhang, Q.; Liu, Z.; Gu, L.; Du, Y.; Huang, W.; Zhang, H. High phase-purity 1T′-MoS_2- and 1T′-$MoSe_2$-layered crystals. *Nat. Chem.* **2018**, *10*, 638−643.
(16) Zhang, X.; Luo, Z.; Yu, P.; Cai, Y.; Du, Y.; Wu, D.; Gao, S.; Tan, C.; Li, Z.; Ren, M.; Osipowicz, T.; Chen, S.; Jiang, Z.; Li, J.; Huang, Y.; Yang, J.; Chen, Y.; Ang, C. Y.; Zhao, Y.; Wang, P.; Song, L.; Wu, X.; Liu, Z.; Borgna, A.; Zhang, H. Lithiation-induced amorphization of $Pd_3P_2S_8$ for highly efficient hydrogen evolution. *Nat. Catal.* **2018**, *1*, 460−468.
(17) Zhou, K.; Zhang, Y.; Xia, Z.; Wei, W. As-prepared MoS^2 quantum dot as a facile fluorescent probe for long-term tracing of live cells. *Nanotechnology* **2016**, *27*, 275101.
(18) Ma, W.; Xu, L.; de Moura, A. F.; Wu, X.; Kuang, H.; Xu, C.; Kotov, N. A. Chiral Inorganic Nanostructures. *Chem. Rev.* **2017**, *117*, 8041−8093.
(19) Moshe, A. B.; Szwarcman, D.; Markovich, G. Size Dependence of Chiroptical Activity in Colloidal Quantum Dots. *ACS Nano* **2011**, *5*, 9034−9043.
(20) Moloney, M. P.; Gun'ko, Y. K.; Kelly, J. M. Chiral Highly Luminescent CdS Quantum Dots. *Chem. Commun.* **2007**, 3900−3902.
(21) Elliott, S. D.; Moloney, M. P.; Gun'ko, Y. K. Chiral Shells and Achiral Cores in CdS Quantum Dots. *Nano Lett.* **2008**, *8*, 2452−2457.
(22) Moloney, M. P.; Govan, J.; Loudon, A.; Mukhina, M.; Gun'ko, Y. K. Preparation of Chiral Quantum Dots. *Nat. Protoc.* **2015**, *10*, 558−573.
(23) Gallagher, S. A.; Moloney, M. P.; Wojdyla, M.; Quinn, S. J.; Kelly, J. M.; Gun'ko, Y. K. Synthesis and Spectroscopic Studies of Chiral CdSe Quantum Dots. *J. Mater. Chem.* **2010**, *20*, 8350−8355.
(24) Zhu, Z.; Guo, J.; Liu, W.; Li, Z.; Han, B.; Zhang, W.; Tang, Z. Controllable Optical Activity of Gold Nanorod and Chiral Quantum Dot Assemblies. *Angew. Chem., Int. Ed.* **2013**, *52*, 13571−13575.
(25) Suzuki, N.; Wang, Y.; Elvati, P.; Qu, Z.-B.; Kim, K.; Jiang, S.; Baumeister, E.; Lee, J.; Yeom, B.; Bahng, J. H.; Lee, J.; Violi, A.; Kotov, N. A. Chiral Graphene Quantum Dots. *ACS Nano* **2016**, *10*, 1744−1755.
(26) Choi, J. K.; Haynie, B. E.; Tohgha, U.; Pap, L.; Elliott, K. W.; Leonard, B. M.; Dzyuba, S. V.; Varga, K.; Kubelka, J.; Balaz, M. Chirality Inversion of CdSe and CdS Quantum Dots without Changing the Stereochemistry of the Capping Ligand. *ACS Nano* **2016**, *10*, 3809−3815.
(27) Evans, C. M.; Cass, L. C.; Knowles, K. E.; Tice, D. B.; Chang, R. P. H.; Weiss, E. A. Review of the Synthesis and Properties of Colloidal Quantum Dots: the Evolving Role of Coordinating Surface Ligands. *J. Coord. Chem.* **2012**, *65*, 2391−2414.
(28) Purcell-Milton, F.; McKenna, R.; Brennan, L. J.; Cullen, C. P.; Guillemeney, L.; Tepliakov, N. V.; Baimuratov, A. S.; Rukhlenko, I. D.; Perova, T. S.; Duesberg, G. S.; Baranov, A. V.; Fedorov, A. V.; Gun'ko, Y. K. Induction of Chirality in Two-Dimensional Nanomaterials: Chiral 2D MoS_2 Nanostructures. *ACS Nano* **2018**, *12*, 954−964.
(29) Valappil, M. O.; Anil, A.; Shaijumon, M.; Pillai, V. K.; Alwarappan, S. A Single-Step Electrochemical Synthesis of Luminescent WS_2 Quantum Dots. *Chem.—Eur. J.* **2017**, *23*, 9144−9148.
(30) Roy, S.; Neupane, G. P.; Dhakal, K. P.; Lee, J.; Yun, S. J.; Han, G. H.; Kim, J. Observation of Charge Transfer in Heterostructures Composed of $MoSe_2$ Quantum Dots and a Monolayer of MoS_2 or WSe_2. *J. Phys. Chem. C* **2017**, *121*, 1997−2004.
(31) Guan, G.; Yang, L.; Mei, Q.; Zhang, K.; Zhang, Z.; Han, M.-Y. Chemiluminescence Switching on Peroxidase-Like Fe_3O_4 Nanoparticles for Selective Detection and Simultaneous Determination of Various Pesticides. *Anal. Chem.* **2012**, *84*, 9492−9497.
(32) Wei, H.; Wang, E. Nanomaterials with Enzyme-Like Characteristics (Nanozymes): Next-Generation Artificial Enzymes. *Chem. Soc. Rev.* **2013**, *42*, 6060−6093.
(33) Cao, G.-J.; Jiang, X.; Zhang, H.; Croley, T. R.; Yin, J.-J. Mimicking Horseradish Peroxidase and Oxidase Using Ruthenium Nanomaterials. *RSC Adv.* **2017**, *7*, 52210−52217.
(34) Qi, C.; Cai, S.; Wang, X.; Li, J.; Lian, Z.; Sun, S.; Yang, R.; Wang, C. Enhanced oxidase/peroxidase-like activities of aptamer conjugated MoS2/PtCu nanocomposites and their biosensing application. *RSC Adv.* **2016**, *6*, 54949−54955.
(35) Sun, Y.; Zhao, C.; Gao, N.; Ren, J.; Qu, X. Stereoselective Nanozyme Based on Ceria Nanoparticles Engineered with Amino Acids. *Chem.—Eur. J.* **2017**, *23*, 18146−18150.
(36) Chen, J. L.-Y.; Pezzato, C.; Scrimin, P.; Prins, L. J. Chiral Nanozymes-Gold Nanoparticle-Based Transphosphorylation Catalysts Capable of Enantiomeric Discrimination. *Chem.—Eur. J.* **2016**, *22*, 7028−7032.
(37) Yin, W.; Yu, J.; Lv, F.; Yan, L.; Zheng, L. R.; Gu, Z.; Zhao, Y. Functionalized Nano-MoS_2 with Peroxidase Catalytic and Near-Infrared Photothermal Activities for Safe and Synergetic Wound Antibacterial Applications. *ACS Nano* **2016**, *10*, 11000−11011.

DOI: 10.1021/acsami.8b10594
ACS Appl. Mater. Interfaces 2018, 10, 30680−30688

(38) Lin, T.; Zhong, L.; Guo, L.; Fu, F.; Chen, G. Seeing diabetes: visual detection of glucose based on the intrinsic peroxidase-like activity of MoS_2 nanosheets. *Nanoscale* **2014**, *6*, 11856−11862.
(39) Wu, J.-Y.; Zhang, X.-Y.; Ma, X.-D.; Qiu, Y.-P.; Zhang, T. High quantum-yield luminescent MoS2 quantum dots with variable light emission created via direct ultrasonic exfoliation of MoS_2 nanosheets. *RSC Adv.* **2015**, *5*, 95178−95182.
(40) Li, F.; Li, J.; Cao, Z.; Lin, X.; Li, X.; Fang, Y.; An, X.; Fu, Y.; Jin, J.; Li, R. MoS_2 quantum dot decorated RGO: a designed electrocatalyst with high active site density for the hydrogen evolution reaction. *J. Phys. Chem. A* **2015**, *3*, 21772−21778.
(41) Jin, H.; Baek, B.; Kim, D.; Wu, F.; Batteas, J. D.; Cheon, J.; Son, D. H. Effects of Direct Solvent-Quantum Dot Interaction on the Optical Properties of Colloidal Monolayer WS_2 Quantum Dots. *Nano Lett.* **2017**, *17*, 7471−7477.
(42) Gu, W.; Yan, Y.; Zhang, C.; Ding, C.; Xian, Y. One-Step Synthesis of Water-Soluble MoS_2 Quantum Dots via a Hydrothermal Method as a Fluorescent Probe for Hyaluronidase Detection. *ACS Appl. Mater. Interfaces* **2016**, *8*, 11272−11279.
(43) Dai, W.; Dong, H.; Fugetsu, B.; Cao, Y.; Lu, H.; Ma, X.; Zhang, X. Tunable Fabrication of Molybdenum Disulfide Quantum Dots for Intracellular MicroRNA Detection and Multiphoton Bioimaging. *Small* **2015**, *11*, 4158−4164.
(44) Hoy, J.; Morrison, P. J.; Steinberg, L. K.; Buhro, W. E.; Loomis, R. A. Excitation Energy Dependence of the Photoluminescence Quantum Yields of Core and Core/Shell Quantum Dots. *J. Phys. Chem. Lett.* **2013**, *4*, 2053−2060.
(45) Sharma, A.; Gadly, T.; Gupta, A.; Ballal, A.; Ghosh, S. K.; Kumbhakar, M. Origin of Excitation Dependent Fluorescence in Carbon Nanodots. *J. Phys. Chem. Lett.* **2016**, *7*, 3695−3702.
(46) Das, S. K.; Luk, C. M.; Martin, W. E.; Tang, L.; Kim, D. Y.; Lau, S. P.; Richards, C. I. Size and Dopant Dependent Single Particle Fluorescence Properties of Graphene Quantum Dots. *J. Phys. Chem. C* **2015**, *119*, 17988−17994.
(47) Knappenberger, K. L.; Wong, D. B.; Xu, W.; Schwartzberg, A. M.; Wolcott, A.; Zhang, J. Z.; Leone, S. R. Excitation-Wavelength Dependence of Fluorescence Intermittency in CdSe Nanorods. *ACS Nano* **2008**, *2*, 2143−2153.
(48) Wang, N.; Wei, F.; Qi, Y.; Li, H.; Lu, X.; Zhao, G.; Xu, Q. Synthesis of Strongly Fluorescent Molybdenum Disulfide Nanosheets for Cell-Targeted Labeling. *ACS Appl. Mater. Interfaces* **2014**, *6*, 19888−19894.
(49) Yang, L. Excitonic Effects on Optical Absorption Spectra of Doped Graphene. *Nano Lett.* **2011**, *11*, 3844−3847.
(50) Devi, S.; Singh, B.; Paul, A. K.; Tyagi, S. Highly Sensitive and Selective Detection of Trinitrotoluene Using Cysteine-Capped Gold Nanoparticles. *Anal. Methods* **2016**, *8*, 4398−4405.
(51) Aryal, S.; B. K. C, R.; Dharmaraj, N.; Bhattarai, N.; Kim, C. H.; Kim, H. Y. Spectroscopic identification of SAu interaction in cysteine capped gold nanoparticles. *Spectrochim. Acta, Part A* **2006**, *63*, 160−163.
(52) Bagbi, Y.; Sarswat, A.; Mohan, D.; Pandey, A.; Solanki, P. R. Lead and Chromium Adsorption from Water using L-Cysteine Functionalized Magnetite (Fe_3O_4) Nanoparticles. *Sci. Rep.* **2017**, *7*, 7672.
(53) Volkert, A. A.; Subramaniam, V.; Ivanov, M. R.; Goodman, A. M.; Haes, A. J. Salt-Mediated Self-Assembly of Thioctic Acid on Gold Nanoparticles. *ACS Nano* **2011**, *5*, 4570−4580.
(54) Furo, T.; Mori, T.; Wada, T.; Inoue, Y. Absolute Configuration of Chiral [2.2]Paracyclophanes with Intramolecular Charge-Transfer Interaction. Failure of the Exciton Chirality Method and Use of the Sector Rule Applied to the Cotton Effect of the CT Transition. *J. Am. Chem. Soc.* **2005**, *127*, 8242−8243.
(55) Brahma, S.; Ikbal, S. A.; Dhamija, A.; Rath, S. P. Highly Enhanced Bisignate Circular Dichroism of Ferrocene-Bridged Zn(II) Bisporphyrin Tweezer with Extended Chiral Substrates due to Well-Matched Host-Guest System. *Inorg. Chem.* **2014**, *53*, 2381−2395.
(56) Ben-Moshe, A.; Teitelboim, A.; Oron, D.; Markovich, G. Probing the Interaction of Quantum Dots with Chiral Capping Molecules using Circular Dichroism Spectroscopy. *Nano Lett.* **2016**, *16*, 7467−7473.
(57) Zhou, Y.; Zhu, Z.; Huang, W.; Liu, W.; Wu, S.; Liu, X.; Gao, Y.; Zhang, W.; Tang, Z. Optical Coupling Between Chiral Biomolecules and Semiconductor Nanoparticles: Size-Dependent Circular Dichroism Absorption. *Angew. Chem., Int. Ed.* **2011**, *50*, 11456−11459.
(58) Tohgha, U.; Deol, K. K.; Porter, A. G.; Bartko, S. G.; Choi, J. K.; Leonard, B. M.; Varga, K.; Kubelka, J.; Muller, G.; Balaz, M. Ligand Induced Circular Dichroism and Circularly Polarized Luminescence in CdSe Quantum Dots. *ACS Nano* **2013**, *7*, 11094−11102.
(59) Tian, J.; Liu, Q.; Asiri, A. M.; Qusti, A. H.; Al-Youbi, A. O.; Sun, X. Ultrathin Graphitic Carbon Nitride Nanosheets: A Novel Peroxidase Mimetic, Fe Doping-Mediated Catalytic Performance Enhancement and Application to Rapid, Highly Sensitive Optical Detection of Glucose. *Nanoscale* **2013**, *5*, 11604−11609.
(60) Bhagi-Damodaran, A.; Michael, M. A.; Zhu, Q.; Reed, J.; Sandoval, B. A.; Mirts, E. N.; Chakraborty, S.; Moënne-Loccoz, P.; Zhang, Y.; Lu, Y. Why Copper is Preferred over Iron for Oxygen Activation and Reduction in Haem-Copper Oxidases. *Nat. Chem.* **2017**, *9*, 257−263.
(61) Silva, C. S.; Durão, P.; Fillat, A.; Lindley, P. F.; Martins, L. O.; Bento, I. Crystal structure of the multicopper oxidase from the pathogenic bacterium Campylobacter jejuniCGUG11284: characterization of a metallo-oxidase. *Metallomics* **2012**, *4*, 37−47.
(62) Xiong, Y.; Qin, Y.; Su, L.; Ye, F. Bioinspired Synthesis of Cu2+-Modified Covalent Triazine Framework: A New Highly Efficient and Promising Peroxidase Mimic. *Chem.—Eur. J.* **2017**, *23*, 11037−11045.
(63) Vázquez-González, M.; Liao, W.-C.; Cazelles, R.; Wang, S.; Yu, X.; Gutkin, V.; Willner, I. Mimicking Horseradish Peroxidase Functions Using Cu^{2+}-Modified Carbon Nitride Nanoparticles or Cu^{2+}-Modified Carbon Dots as Heterogeneous Catalysts. *ACS Nano* **2017**, *11*, 3247−3253.
(64) Gao, L.; Zhuang, J.; Nie, L.; Zhang, J.; Zhang, Y.; Gu, N.; Wang, T.; Feng, J.; Yang, D.; Perrett, S.; Yan, X. Intrinsic Peroxidase-Like Activity of Ferromagnetic Nanoparticles. *Nat. Nanotechnol.* **2007**, *2*, 577−583.
(65) Hayashi, Y.; Santoro, S.; Azuma, Y.; Himo, F.; Ohshima, T.; Mashima, K. Enzyme-Like Catalysis via Ternary Complex Mechanism: Alkoxy-Bridged Dinuclear Cobalt Complex Mediates Chemoselective O-Esterification over N-Amidation. *J. Am. Chem. Soc.* **2013**, *135*, 6192−6199.
(66) Wei, W.; Wu, L.; Xu, C.; Ren, J.; Qu, X. A General Approach Using Spiroborate Reversible Cross-Linked Au Nanoparticles for Visual High-Throughput Screening of Chiral Vicinal Diols. *Chem. Sci.* **2013**, *4*, 1156−1162.
(67) Johannsmann, D.; Reviakine, I.; Rojas, E.; Gallego, M. Effect of Sample Heterogeneity on the Interpretation of QCM(-D) Data: Comparison of Combined Quartz Crystal Microbalance/Atomic Force Microscopy Measurements with Finite Element Method Modeling. *Anal. Chem.* **2008**, *80*, 8891−8899.
(68) Zhao, K.; Gu, W.; Zheng, S.; Zhang, C.; Xian, Y. SDS-MoS_2 nanoparticles as highly-efficient peroxidase mimetics for colorimetric detection of H_2O_2 and glucose. *Talanta* **2015**, *141*, 47−52.

DOI: 10.1021/acsami.8b10594
ACS Appl. Mater. Interfaces 2018, 10, 30680−30688